ADVANCED FUNCTIONAL MATERIALS
www.afm-journal.de

Colloidal Crack Sintering Lithography for Light-Induced Patterning of Particle Assemblies

Marius Schoettle, Ariane V. Mader, and Willem L. Noorduin**

Photoinduced patterning can generate intricate topographic structures, but it relies heavily on specialized materials, which limits its general usability. Here, colloidal crack sintering lithography (CCSL) is introduced, a patterning method based simply on a commodity polymer and water that interact with focused near-infrared light. Photothermal heating causes nanoscale sintering in polymer colloidal assemblies, which in turn induces controlled formation of cracks on the micron scale. Because light provides spatiotemporal control, individual cracks can be guided along precisely defined trajectories. Furthermore, this photo-driven sintering mechanism can be applied to subsequently convert such cracks into an open channel morphology. The result is reminiscent of positive resists in photolithographic patterning, as the precursor material is selectively removed along the irradiated path. Consequently, CCSL provides analogous functionality to photolithography in templating techniques such as shadow masks in physical vapor deposition and templated colloidal self-assembly.

1. Introduction

Patterning surfaces with complex topographies often requires controlled assembly processes, especially when this topography approaches the nanoscale.[1–3] One such self-organizing system is the spontaneous formation of crack networks.[4] While crack formation is typically considered as an undesired failure mode, many groups have recognized the opportunities presented by controlled cracking.[5,6] Typical systems include cracking due to a mismatch in the thermal expansion coefficient,[7] mismatch of the elastic modulus,[8] and drying-induced stress.[9]

Perhaps the most prominent type of crack pattern is the interconnected, random network found in geological formations such as rocks or dried lake beds.[10] Analogous random patterns can be realized in thin films by vapor deposition[11] or in drying latex suspensions,[12] e.g., for templating transparent electrodes.[13,14] Complementary to random patterns, anisotropic properties can be achieved by directing crack propagation with pre-patterned substrates[15] or adjusted colloidal mixtures.[12,16] For example, Odziomek et al. recently established equidistant, parallel cracks and their use as responsive diffraction gratings.[17]

While extended crack networks are ideal for creating homogeneous patterns over large areas, other applications, such as active electronics[18] require more intricate structures and local control. An ideal trigger for such spatial control is light,[19–22] which has been applied in the patterning of various hard[23] and soft materials.[24,25] Light has also been shown to locally change the orientation of cracks in systems such as liquid crystals,[26] and photothermally controlled evaporation rates in colloidal suspensions.[27]

The highest degree of spatial control achievable is the initiation of a single crack and guiding the propagation along a defined trajectory. This level of control has only been shown in photolithography-based methods.[28,29] In this "crack lithography", gradient photoresists and double exposure result in the local concentration of stress and controlled formation of individual cracks.[30] However, this specialized and expensive procedure also means that the use cases are limited.

Of the previously mentioned self-organized cracking strategies, the ones based on colloidal assemblies are the least technical and, therefore, most generalizable. So far, these all result in a network of cracks, and it would be highly beneficial to detect a mechanism that creates and controls individual cracks with multidirectional control. Here, we establish such a system with control over individual cracks based on post-assembly manipulation of colloidal thin films. Local, photothermal heating causes confined sintering of the particulate nanostructure,[31] which in turn induces controlled cracking. Furthermore, we find that the same mechanism can be used to locally sinter the area around cracks, creating an open channel morphology that is accessible for templating procedures. Collectively, these strategies enable the rational production of increasingly complex motifs, combining straight lines as well as curves, and offer direct writing of 2D

M. Schoettle, A. V. Mader, W. L. Noorduin
AMOLF
Science Park 104, Amsterdam 1098 XG, The Netherlands
E-mail: schoettle@amolf.nl; noorduin@amolf.nl
A. V. Mader, W. L. Noorduin
Van't Hoff Institute for Molecular Sciences
University of Amsterdam
Amsterdam 1090 GD, The Netherlands

The ORCID identification number(s) for the author(s) of this article can be found under https://doi.org/10.1002/adfm.202520056

DOI: 10.1002/adfm.202520056

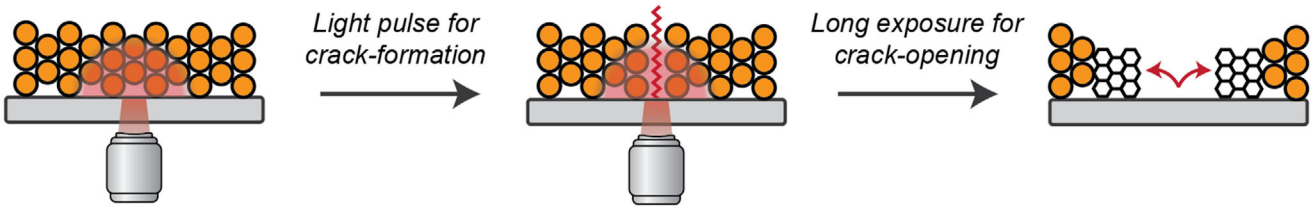

Scheme 1. Principle of colloidal crack sintering lithography. 1) Short, local heating causes controlled crack formation. 2) Longer heating induces crack-opening.

structures. Since this strategy combines the characteristic advantages of selective laser sintering and crack-lithography, we name this method colloidal crack sintering lithography (CCSL).

2. Results

The principle of CCSL is based on photothermal heating, which causes spatially confined sintering in colloidal assemblies. In this work, we show how sintering and nanoscale rearrangement can cause 1) controlled crack formation, and 2) opening of already formed cracks (**Scheme 1**). Monodisperse copolymer colloids are synthesized through surfactant-free emulsion polymerization of a mixture of methyl methacrylate (MMA) and *n*-butyl acrylate (nBA). Throughout this study, colloidal thin-films consisting of these particles are subjected to elevated temperatures, which trigger the sintering process and the emergent reorganization and patterning.

In our CCSL approach, focused near-infrared (NIR) radiation in combination with water as a sensitizer supplies the controlled energy input needed for local sintering.[32] The system is prepared by evaporation-induced self-assembly of polymer colloids on a flat substrate, which is subsequently immersed in water inside a closed cell. In our custom setup,[33] a NIR laser beam (λ = 1435 nm) is focused on the sample surface (**Figure 1a**). The selected wavelength coincides with the first overtone of the O-H stretch vibration in H_2O,[34] resulting in localized resonant heating. The generated heat is transferred to the polymer, locally increasing the temperature above the glass transition temperature (T_g) (Figure S1, Supporting Information). A standard epi-illumination microscope, mounted from the opposite side of the setup, provides in situ monitoring of the concomitant sintering process.

Sintering-induced cracking has so far only been considered a nuisance, and existing research is focused on mitigation strategies.[35–38] Here, we test how we can guide this process and build user-defined crack patterns by localization of sintering-induced stress and controlled crack formation (Figure 1b). The polymer colloids are assembled on a hydrophobic substrate, and the resulting thin film is transferred to an adhesive layer before assembling the cell. We begin with a low laser intensity of 50 mW and target a spot on the thin-film for a duration of 1 s. This immediately causes a linear crack to form between the edge of the domain and the sintered spot. This process can be repeated sequentially, causing secondary cracks to branch off from the first (Figure 1c; Figure S2, Supporting Information). The same branched shape, mirrored along the x-axis, can also be generated from the opposite edge of the colloidal assembly. This high degree of multidirectional control is due to the inherently self-limiting nature of the linear cracks, as sintering of colloids in the irradiated spot prevents further propagation of the crack and creates a natural stopping point (Figures S3 and S4, Supporting Information).

Next, we examine the effect of a higher laser power. The power is increased to 80 mW, while the irradiation time remains 1 s. This causes the formation of a semi-circular crack in the colloidal film around the irradiated spot (Figure 1d; Figures S5 and S6, Supporting Information). Such a curved crack can be extended to an almost complete circle via secondary irradiation at a higher power, which intensifies the densification and induces crack propagation (Figure S7, Supporting Information).

The two modes of cracking that were distinguished here are attributed to the difference in laser power and its influence on the sintered area. (i) For irradiation with low laser power, the area that is heated above the polymer T_g is comparatively small, such that built-up stress dissipates by forming linear cracks between the edge of the domain and the sintered spot. (ii) Conversely, for irradiation with high laser power, a larger area is heated above the polymer T_g, and densification and contraction result in an isotropic response, where a semi-circular crack forms around the irradiated spot.

With this control over sintering-induced crack formation in place, we examine the possibility of more complex structural motifs via sequential cracking. For example, if a semi-circular crack is formed close to a domain edge, it will immediately be connected to linear cracks to the edges as well (Figure 1e). Alternatively, two consecutive irradiated spots can also result in combined crack motifs. A semi-circular crack can be extended by a linear crack (Figure 1f) or a second semi-circle to form an S-shape (Figure 1g; Figure S8, Supporting Information). Since the energy barrier for crack propagation is lower than the formation of a new crack, the two motifs connect perfectly. This possibility of combining structural motifs and creating increasingly complex patterns with spatiotemporal control makes CCSL a versatile direct writing technique.

Having established controlled crack-formation, we realize that further restructuring has the potential to increase the versatility of this topological pattern. Controlled opening of cracks to form microchannels could make them accessible for various templating or microfluidic techniques. We further realize that such a reorganization can be achieved using the same sintering mechanism, where a decrease of the effective density causes shrinkage and lateral material transport (**Figure 2a**). The only difference between crack opening and crack formation is that for crack opening, the elevated temperature must be applied longer.

As a proof of principle, we examine sintering-induced opening of naturally occurring cracks that originate from the

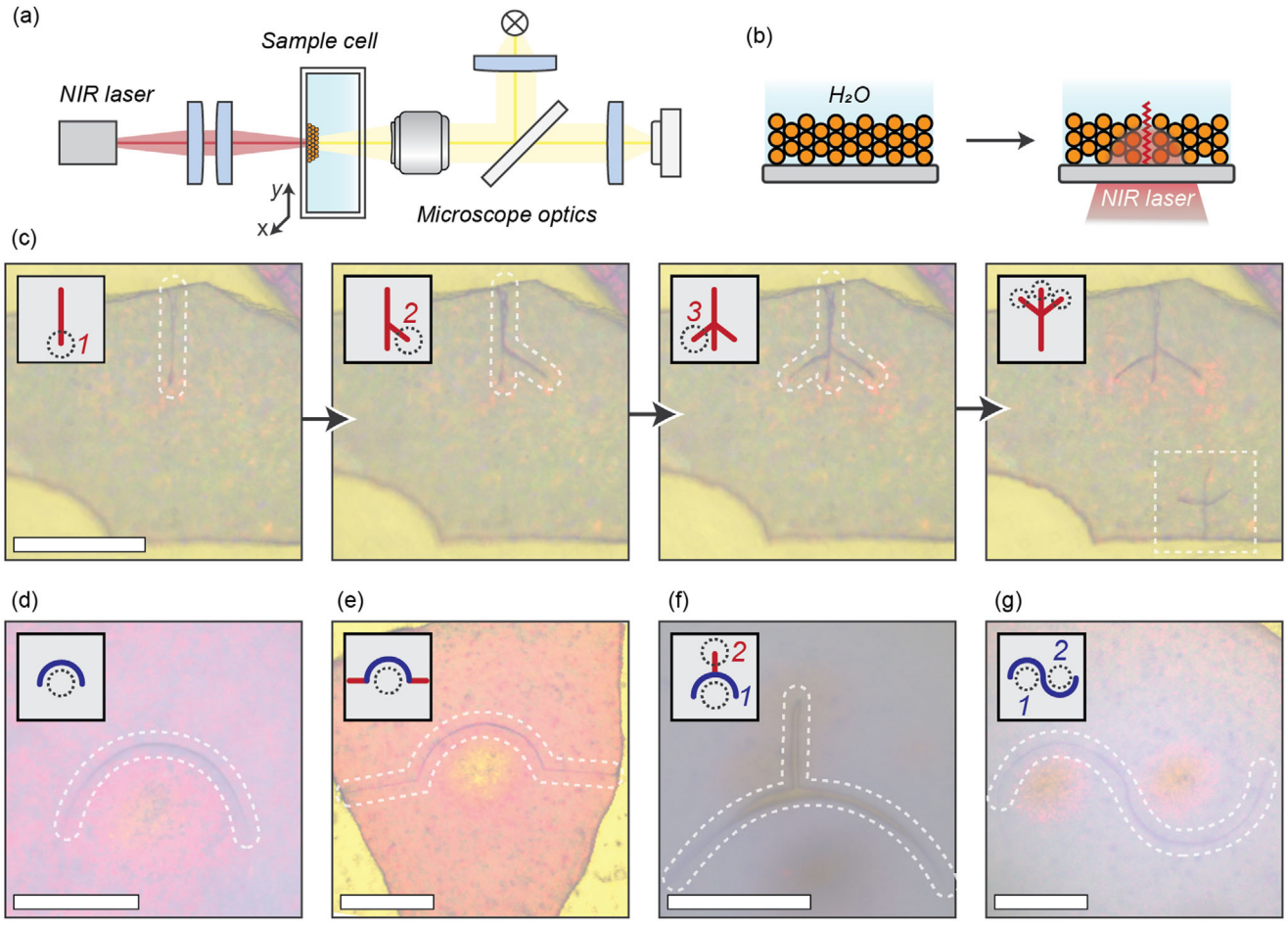

Figure 1. Local sintering and generation of cracks. a) Schematic optical setup for local resonant heating and in situ microscopy. b) Schematic crack formation caused by photothermal heating and sintering-induced stress in the colloidal thin-film. c) Successive generations of linear cracks branching out from each other. d) Semicircle crack generated with higher laser power. e–g) Crack motifs obtained from various combinations of linear and circular cracks, some with two consecutive irradiation spots. The dotted circles in the insets indicate where the samples were irradiated. Scale bars are 200 µm.

self-assembly process. Evaporative colloidal assembly on hydrophilic substrates results in a thin film with an overall orange appearance at normal incidence due to constructive interference of light reflected from the photonic colloidal crystal. Additionally, a random crack network can be seen as dark lines due to light scattering at the edges of the crystalline domains (Figure 2c). These cracks originate from drying-induced stress, and scanning electron microscopy (SEM) images show a sub-µm crack width (Figure 2e).

In preliminary experiments, we induce crack-opening by heating the entire sample globally. A temperature of 100 °C, which is above the T_g of the constituent particles (Figure 2b), causes deformation and sintering via polymer creep.[39,40] This plasticity has a direct effect on the photonic properties.[41] Air is expelled from the interstitial pores and the periodic structure is transformed into a dense polymer, leading to the loss of structural coloration (Figure 2d; Figure S9, Supporting Information). This nanoscale rearrangement also has implications on the microscopic scale. As the effective density of the material increases, the domains simultaneously shrink. Lateral material transport thereby opens the preformed cracks to a width of several micrometers (Figure 2f; Figure S10, Supporting Information). The main driving force behind this process is the polymer-air surface tension,[42] which results in bulk polymer domains with some residual nanoscale topography (Figure S11, Supporting Information).

We further elucidate the fundamental mechanism of crack opening using in situ scanning electron microscopy studies (Figure 2g; Figure S12, Supporting Information). Here, the electron beam is simultaneously used for imaging as well as energy input to trigger local sintering. While electron beam-induced sintering would usually be regarded as an unwanted artifact, here it shows how, within seconds, the deformation and densification of the particulate assembly cause overall mass transport and crack opening. Some particles continue to bridge the gap between domains and are severely deformed. However, in the case of a fully sintered film, such as in Figure 2f, where the cracks are opened much further, the deformed particle strands break, and this bridging is no longer observed. This in situ data shows how nanoscale polymer particle deformation can drive controlled reorganization on a micron scale, and indicates that this phenomenon can also be triggered with local control.

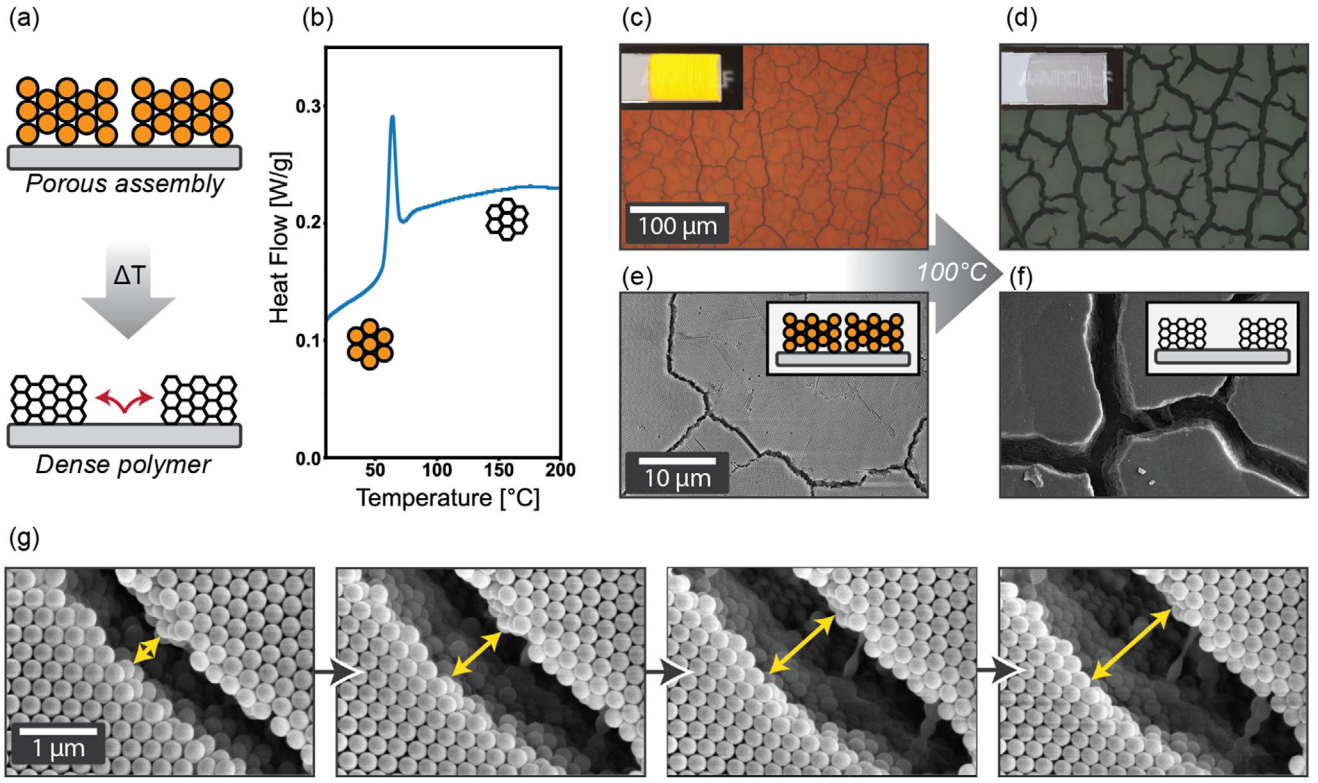

Figure 2. Colloidal crack sintering. a) Sintering and densification cause the opening of cracks and generate an open channel morphology. b) DSC thermogram of the copolymer particles showing a glass transition at 54 °C. c,d) Optical microscopy images of a colloidal crystal before and after heating to 100 °C, respectively. Insets show photographs of dip-coated samples exposed to the same temperatures and a visible change from orange to translucent. e,f) SEM images of the same samples with insets showing schematic representations of the underlying structure. g) In situ SEM images of an opening crack triggered by electron beam-induced sintering.

To showcase the opportunities presented by the open channel morphology, we use these in various templating protocols, starting with simply assembling colloids inside the opened cracks. To this end, a colloidal crystal is first completely sintered via global heating and then is re-immersed in the original particle suspension and slowly withdrawn using a dip-coating procedure (**Figure 3a**). Capillary forces and evaporation-induced self-assembly result in a new, densely packed colloidal crystal with hexagonal symmetry confined within the opened crack pattern (Figure 3b).[43,44] The periodically arranged particles extend even into the tapered ends of dead-end cracks (Figure S13, Supporting Information). Different types of extended crack structures can now be created, opened, and backfilled this way. To highlight this, the crack network morphology of the initial colloidal assembly is varied from interconnected random cracks to parallel lines by adjusting the particle polydispersity,[16] without changing the thermal properties (Figures S14 and S15, Supporting Information). These opened crack networks can be backfilled via dip-coating, which results in a photonic colloidal crystal directed by a superstructure of choice (Figure 3c,d; Figure S16, Supporting Information). Opened channels with a width and height of ≈10 × 10 µm are homogeneously filled by this process (Figure S17, Supporting Information), showing how sintering-induced crack opening can direct self-assembly. The driving forces that ensure selectivity during dip-coating are: 1) Capillary action during the vertical deposition from aqueous suspension due to the confined space in the opened cracks. 2) An inherent wettability contrast between the hydrophobic polymer and the hydrophilic surface of the underlying glass substrate, which is locally exposed via crack opening.[43,45]

The applied copolymer also allows for a second thermal processing step. By increasing the temperature to 200 °C, the viscosity of the material can be lowered to a degree that allows polymer flow to close the previously opened cracks completely (Figure S18, Supporting Information). The possibility of opening and subsequently closing a crack network suggests that this system could be used to first fill the cracks and then encapsulate the incorporated compound. Thereby, the filler would be both patterned and passivated.

Here, we provide a proof of principle of this passivation step using as filler lead halide perovskite semiconductors (Figure 3e). These perovskites are widely studied and easily traceable via fluorescence. They are also known to be very susceptible to decomposition when brought in contact with air and water,[46] which makes passivation by encapsulation desirable. To demonstrate the patterning concept, we assemble polymer particles together with lead acetate in the cracks (Figure S19, Supporting Information). After deposition, this precursor is converted into a photoluminescent lead halide perovskite by reacting with a solution of methyl ammonium bromide.[47] Subsequent thermal annealing encapsulates the filler in the resulting polymer film and passivates the perovskite against water-induced decay, even after

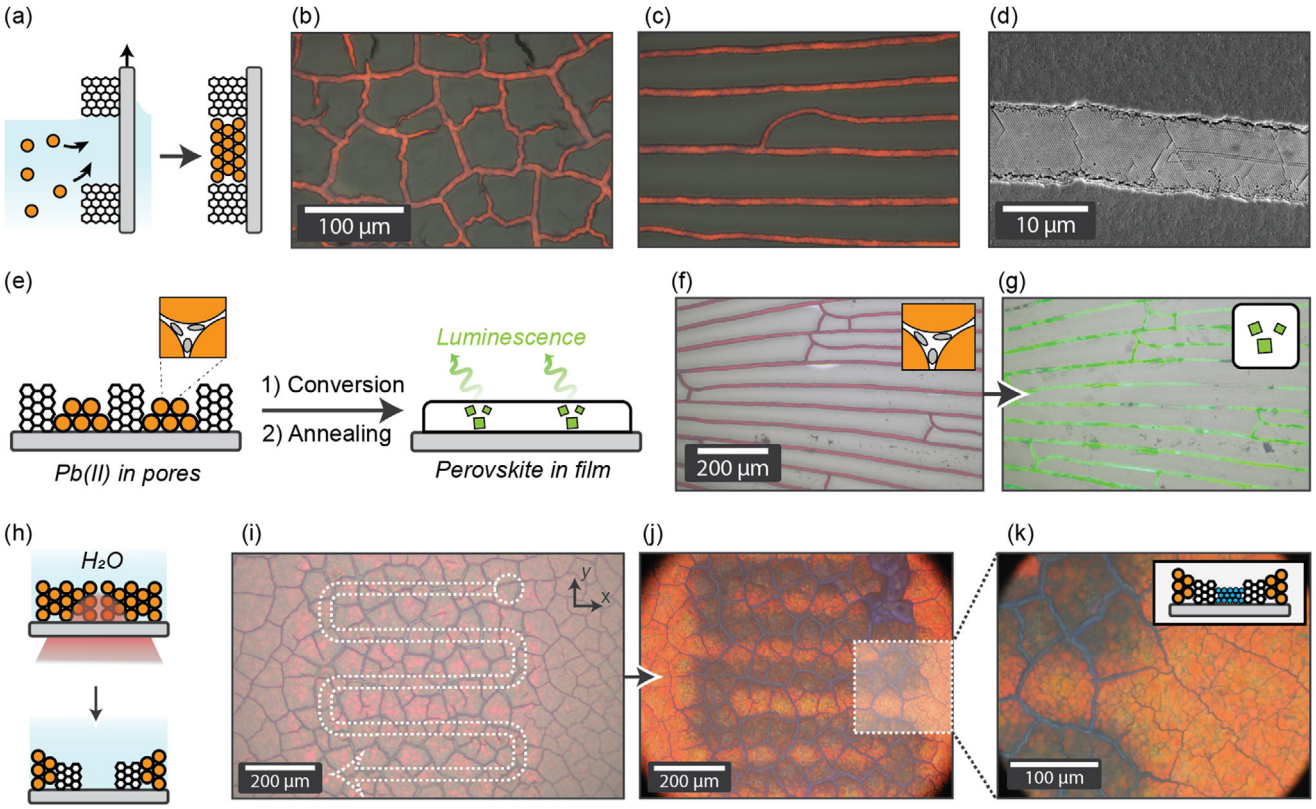

Figure 3. Templating with open crack networks. a) Schematic dip-coating process used for backfilling opened cracks with polymer particles. b,c) Optical microscopy images of backfilled samples where the crack morphology was adjusted to random or parallel, respectively. d) SEM image of a backfilled channel. e) Schematic co-assembly of a lead precursor and polymer colloids in the opened channels, with subsequent conversion to a lead halide perovskite and polymer annealing to encapsulate the perovskite. f) Optical microscopy image of cracks backfilled with a colloidal crystal and lead acetate. g) Fluorescence microscopy of photoluminescent perovskites in the annealed film after immersion in water, showing that the perovskites remain intact. h) Schematic local sintering and opening of cracks in areas illuminated by NIR-light. i) Colloidal crystal, immersed in water, with cracks locally opened in a square area by scanning the NIR-laser spot. j,k) Optical microscopy images of the same sample after backfilling with smaller particles.

immersion in water for several days (Figure 3f,g; Figure S20, Supporting Information).

Alternatively to encapsulation, templating procedures can be chosen where the polymeric template is removed via calcination or dissolution to leave behind a structured inorganic material. We show this possibility by creating replica of the crack network in the form of silica (Figure S21, Supporting Information), as well as an interconnected gold mesh (Figure S22, Supporting Information). Cracks can thus be opened and closed to encapsulate or replicate complex, user-defined patterns.

This crack opening can also be induced with local control. We photothermally trigger the sintering-induced crack opening with the custom microscope (Figure 3h). The laser spot is scanned along the surface of a cracked colloidal assembly in a square area with a side length of 600 µm (Figure 3i). Similar to the previous experiments, sintering-induced crack opening ensues, now confined within the square area. These locally opened cracks allow for the use of the same templating procedures developed earlier for globally opened cracks. To show this, smaller particles are filled into the trenches via dip-coating, which now appear blue due to the shifted photonic stop band (Figure 3j). Close-ups show that this effect is indeed limited to the irradiated area and cracks that were not subjected to local sintering remain largely unaffected during the backfilling process (Figure 3k; Figure S23, Supporting Information).

Motivated by these results, we explore how to maximize the spatial control during crack opening by targeting only one crack at a time and tracing the laser along its trajectory. The laser thereby allows us to open exactly one crack instead of the entire network. Therefore, we induce self-assembly of the polymeric colloids on hydrophobic substrates to increase the natural spacing between drying-induced cracks to several 100 µm to match the laser resolution. To demonstrate the opening of individual cracks, the colloidal assembly is immersed in water and scanned to select a specific crack. Once the trajectory is defined, the laser is moved along it with a scanning speed of 15 µm sec^{-1} at a laser power of 80 mW. This causes the crack to gradually open into a predefined microchannel (**Figure 4a**; MovieS1, Supporting Information). The blueshift in the microscopy image that accompanies the crack opening along the path of the laser is consistent with a local deformation-induced reduction of the spacing in the periodic nanostructure. When moving through junctions in the network, cracks in other directions also open to a small degree (Figure 4b). Nevertheless, the targeted trajectory can clearly be recognized in the final open channel.

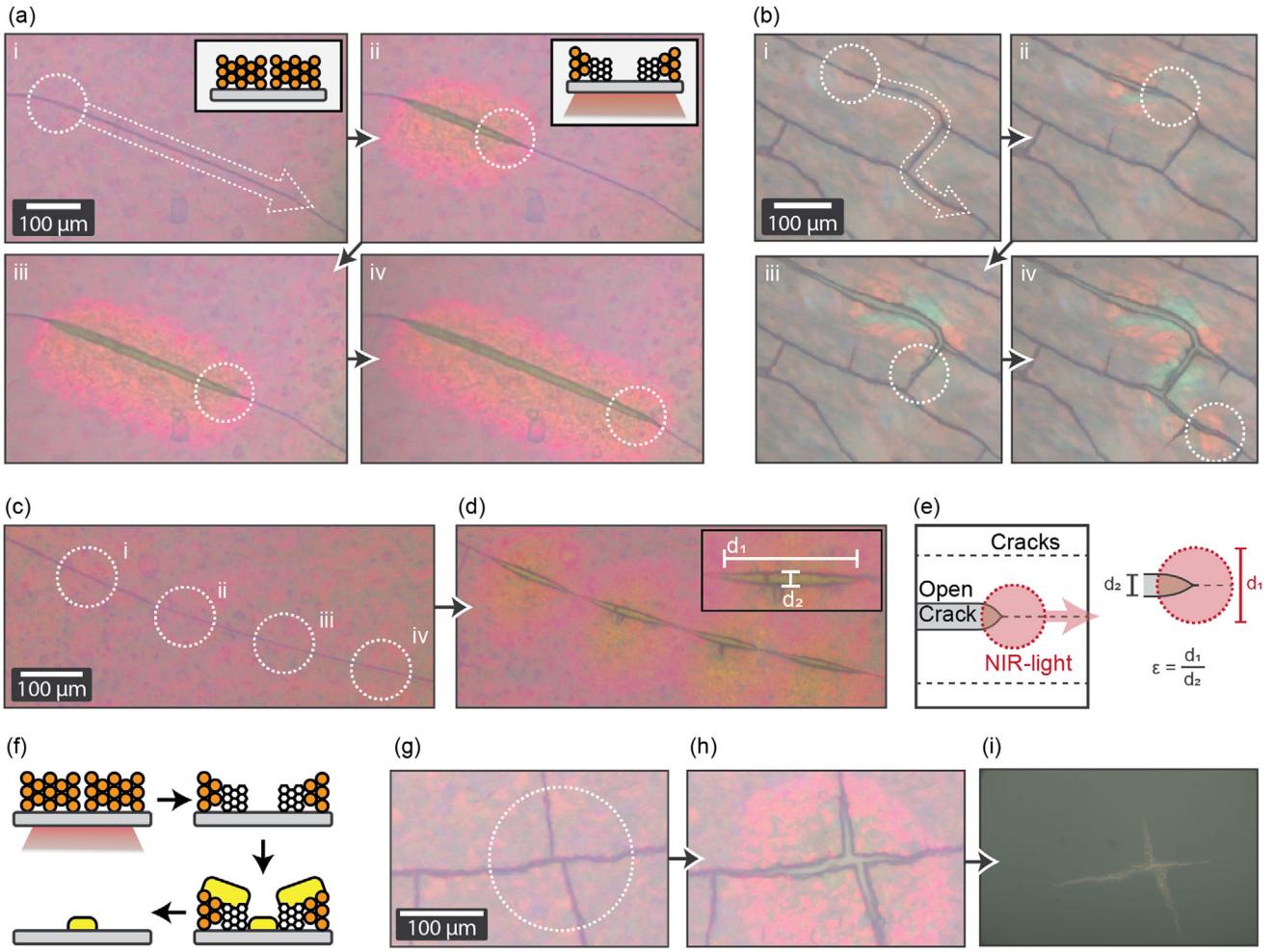

Figure 4. Selective opening of specific cracks. a,b) In situ microscopy data obtained during the selective opening of a crack along predefined paths. c,d) Pointwise local sintering at equidistant positions, resulting in an undulating width of the opened crack. e) Schematic of how the combination of a laser spot and the crack opening synergistically enhances the patterning resolution. f) Schematic gold masking process. g,h) Local opening of a crack junction. i) Gold replica obtained by using the opened junction as a mask during sputter coating.

CCSL can also be used to create more complex channel morphologies. For example, when a linear crack is irradiated at equidistant positions along its length, an undulating channel width can be realized (Figure 4c,d). These individual lens shapes also elucidate another advantage of CCLS: upon irradiation, the targeted crack will open to a width of only a few microns, which is much less than the resolution of the heated spot (>100 µm). This downscaling can be seen as a synergistic enhancement of the patterning resolution (Figure 4e). As a means of quantifying this, we define a resolution enhancement factor ϵ as the ratio of the sintered spot diameter and the opened crack width. Since the area of effect of the laser beam corresponds to the length of the lens shape, the aspect ratio of the lens equals ϵ (Figure 4d inset). A length of 128 ± 10 µm and a width of 11 ± 1 µm give an enhancement factor of $\epsilon = 11.4 \pm 0.7$ for our system. This effect creates micron-sized channels, such that structures fall in the range of what is often targeted for microfluidics.

An additional opportunity of CCSL is the use of open crack structures as masks for vapor-phase deposition, such as metal sputtering. The localized opening of cracks via NIR irradiation functions similarly to positive resists in photolithography, where exposure leads to selective material removal. Following local crack opening, a thin gold layer can be deposited over the structure by sputter coating. Subsequent removal of the underlying polymer, along with any overlying metal, reveals the deposited pattern that precisely follows the geometry of the opened cracks (Figure 4f). For example, targeting a crack junction with a circular laser spot produces a cross-shaped opening, which, after sputtering and polymer removal (Figure S24, Supporting Information), results in a corresponding gold cross on the glass substrate (Figure 4g–i). Other geometries, such as linear and U-shaped patterns, are equally feasible (Figures S25–S27, Supporting Information).

Finally, we show how both aspects of CCSL can be combined in a modular approach. A selected crack motif can be formed in a colloidal assembly via photothermally-induced stress. Then, the same NIR-trigger can be applied for crack opening (**Figure 5**; Figure S28, Supporting Information). Thereby, a single

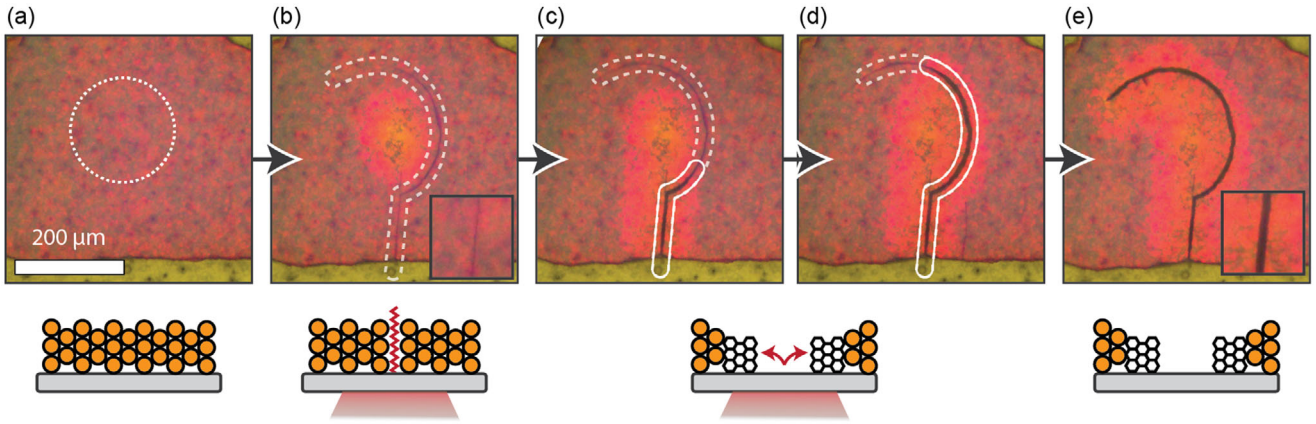

Figure 5. Sequential combination of crack formation and opening. a,b) A short laser pulse induces a semicircular crack connected to a linear crack. c,d) Further sintering along the trajectory of the newly formed crack causes crack opening. e) The final opened a crack.

crack is created along a user-defined trajectory and subsequently converted into an open channel morphology. Importantly, after the patterning and subsequent drying, this structure remains stable for at least several months when stored under standard conditions (Figure S29, Supporting Information). Due to the precisely adjusted glass transition temperature, no further unwanted rearrangement is observed or to be expected.

Separately controlling the formation and opening of cracks provides possibilities for using CCSL to create tailored masks and templates in structure-directing applications. Such use cases would specifically benefit from the spatial freedom and multidirectional control. CCSL also promises tunability by changing the initial colloidal mixture. If a fraction of high-T_g particles were added, this would reduce the degree of sintering and thereby reduce the extent of the lateral movement, resulting in narrower channels. Conversely, an increased porosity of the film via polydisperse colloidal mixtures or hollow spheres could cause the opposite effect and produce wider channels. Besides these nanoscopic properties, the microscopic architecture of the initial thin film presents a multitude of conceivable screening parameters. For example, controlled, extended crack networks could be created during drying,[9,12,17] and used as a precursor to make use of different domain sizes and edges. This makes CCSL fully complementary to existing research on cracking in colloidal assemblies.

For future work we therefore also envision this process as a cost-effective alternative to photolithography. This could find direct application in the fabrication of microfluidic channels, especially considering that straight channels, junctions, and undulating channels (reminiscent of microfluidic mixing channels) are available. For this, an intermediate step that mechanically stabilizes the colloidal assembly would be followed by structural replication with PDMS or epoxy resin. Upscaling such patterning based on CCSL would be feasible by using an adjusted assembly method for larger areas, such as was shown via spray-coating for solar-cell coatings,[48] and faster, automated laser scanning. The accessibility and the competitive resolution will make CCSL a valuable addition to the patterning toolbox. Where other photoinduced patterning techniques require highly specialized materials,[49–51] CCSL is a complementary[52] self-organization process, based only on a commodity polymer, and can inherently be integrated in aqueous systems.

3. Conclusion

We introduced the concept of colloidal crack sintering lithography (CCSL), where photothermal heating via near-infrared absorption caused sintering in colloidal assemblies. This spatially confined, nanoscale reorganization could generate stress in the assembly, which was released via controlled crack formation on the micron scale. By spatially confining the heat input, light serves not only as a trigger but also a guide for directing the initiation and propagation of individual cracks. This approach enables a direct-writing strategy with high spatial precision, allowing for the fabrication of linear, curved, and complex branched patterns with multidirectional control.

In addition, CCSL could be used to convert the newly generated cracks into an open channel morphology. We showed how further sintering caused pronounced densification, which resulted in lateral material transport and opening of cracks. These opened cracks could then be applied in templating techniques such as guided self-assembly or masking during vapor phase metal deposition.

The possibility of using light to trigger a process that selectively removes material from a targeted path is reminiscent of positive resists in photolithographic patterning. We foresee similar use cases of CCSL, e.g., for inexpensive masters in the fabrication of microfluidic chips. Furthermore, since the process is entirely water-based, these structural changes could also be examined in situ in biological systems or inorganic crystallization in confinement.

4. Experimental Section

Materials: Methyl methacrylate (MMA), *n*-butyl acrylate (nBA), 3-styrenesulfonic acid sodium salt hydrate (NaSS, 99%), potassium persulfate (KPS, 99%), and Ludox HS40 silica particles were obtained from Sigma–Aldrich, Lead acetate (>99%) from Thermo Fischer, and methylammonium bromide (98%) from Greatcell Solar. Before further use, both

MMA and nBA were destabilized over Alox B. Deionized water was used throughout all experiments. Glass substrates were cleaned via sonication in an aqueous 2 vol.% Helmanex III solution and in ethanol.

Sample Preparation: Particles were synthesized via surfactant-free emulsion polymerization. Either 15 mL (large particles) or 8 mL (small particles) of a 70:30 mixture of MMA and nBA was added to 240 mL of water and heated to 80 °C under a nitrogen stream for 60 min. Subsequently, 10 mg NaSS in 5 mL water and, 5 min later, 200 mg KPS in 5 mL water were added while stirring. After 120 min, the reaction was terminated by exposure to ambient oxygen. Assembly of colloidal crystals and colloidal glasses proceeded by drop casting 10–20 µL of a monodisperse or mixed particle suspension on a glass substrate at 50 °C. For larger domains, this assembly proceeded on glass hydrophobized via contact with PDMS. Immobilized domains were achieved by self-assembly on a PET foil, after which domains of the colloidal assembly could be transferred to double-sided Kapton tape with a wet cotton tip.

Crack Generation and Opening: Global crack opening proceeded by heating the substrate to 100 °C on a hotplate for 10 min. For local crack generation and opening, the coated substrate and an empty substrate were pressed to either side of a 3 mm thick Viton spacer, thereby creating a cell that was subsequently filled with water. After letting the cell sit for 24 h to allow trapped air to escape the porous structure, the cell was placed inside a custom-built microscope. This microscope consists of an epi-illumination part with a white light LED from one side and a 1435 laser diode, that was collimated and focused by two plano-convex lenses, from the other side.[33] For crack opening, a laser power of 80 mW was used, and for the crack generation either 50 mW ("low" power) or 60–120 mW ("high" power).

Templating: Backfilling of opened cracks proceeded by dipping the substrate in a 1.0 wt.% dispersion of polymer particles and extracting it at 2 µm $^{-1}$s at room temperature. For the co-assembly with the perovskite, 0.01 wt.% lead acetate was added to the coating suspension. Development then proceeded by dipping a tissue in a 0.16 M solution of methylammonium bromide in isopropyl alcohol and stamping this on the sample surface. The sample was subsequently heated at 100 °C for 10 min and immersed in water for 72 h for the stability analysis. Backfilling with silica particles proceeded similarly, with a 1.0 wt.% dispersion of Ludox HS40. The polymer was subsequently removed by holding the backside of the substrate in the blue flame of a Bunsen burner. Gold deposition through the opened cracks was done in a Leica EM ACE600 sputter coater, where a film of 20 nm thickness was deposited. Here, the polymer was removed by sonication in water for 20 s and subsequent washing with acetone.

Characterization: Light microscopy was performed with a Leica DMLP in epi-illumination. The combined light and fluorescence microscopy was performed with the custom setup,[23] where a white light LED and a 365 nm UV LED simultaneously illuminated the sample in epi-illumination. Scanning electron microscopy images were obtained with a FEI Verios 460 microscope at an acceleration voltage of 5 kV and an SE detector after sputtering 10 nm of gold on the sample. Differential scanning calorimetry was conducted with a DSC25 by TA Instruments with a heating and cooling rate of 10 K min^{-1}. The particle size distributions were obtained with a Malvern Mastersizer 3000.

Supporting Information

Supporting Information is available from the Wiley Online Library or from the author.

Acknowledgements

H. Schoenmaker is thanked for technical support. Scanning electron microscopy was performed at the fabrication and characterization facilities of the Amsterdam NanoLab, supported by NWO.

Conflict of Interest

The authors declare no conflict of interest.

Data Availability Statement

The data that support the findings of this study are available from the corresponding author upon reasonable request.

Keywords

colloids, cracks, light-controlled patterning, microfabrication, self-organization

Received: August 1, 2025
Revised: September 2, 2025
Published online:

[1] H. Cölfen, S. Mann, *Angew. Chem., Int. Ed.* **2003**, *42*, 2350.
[2] N. Vogel, M. Retsch, C.-A. Fustin, A. Del Campo, U. Jonas, *Chem. Rev.* **2015**, *115*, 6265.
[3] J. Brunner, I. A. Baburin, S. Sturm, K. Kvashnina, A. Rossberg, T. Pietsch, S. Andreev, E. Sturm, H. Cölfen, *Adv. Mater. Interfaces* **2017**, *4*, 1600431.
[4] K. H. Nam, I. H. Park, S. H. Ko, *Nature* **2012**, *485*, 221.
[5] Y. D. Suh, J. Kwon, J. Lee, H. Lee, S. Jeong, D. Kim, H. Cho, J. Yeo, S. H. Ko, *Adv. Electron. Mater.* **2016**, *2*, 1600277.
[6] K. R. Phillips, C. T. Zhang, T. Yang, T. Kay, C. Gao, S. Brandt, L. Liu, H. Yang, Y. Li, J. Aizenberg, L. Li, *Adv. Funct. Mater.* **2020**, *30*, 1908242.
[7] V. H. Nguyen, D. T. Papanastasiou, J. Resende, L. Bardet, T. Sannicolo, C. Jiménez, D. Muñoz-Rojas, N. D. Nguyen, D. Bellet, *Small* **2022**, *18*, 2106006.
[8] B. Zhang, J. Lei, D. Qi, Z. Liu, Y. Wang, G. Xiao, J. Wu, W. Zhang, F. Huo, X. Chen, *Adv. Funct. Mater.* **2018**, *28*, 1801683.
[9] F. Thorimbert, A. Brachfeld, M. Odziomek, C. Boissière, H. Amenitsch, D. Naumenko, G. Mattana, N. Baccile, M. Faustini, *Adv. Mater. Technol.* **2024**, *9*, 2400353.
[10] T. R. Astin, D. A. Rogers, *J. Sediment. Res.* **1991**, *61*, 850.
[11] K. D. M. Rao, R. Gupta, G. U. Kulkarni, *Adv. Mater. Interfaces* **2014**, *1*, 1400090.
[12] O. Dalstein, E. Gkaniatsou, C. Sicard, O. Sel, H. Perrot, C. Serre, C. Boissière, M. Faustini, *Angew. Chem., Int. Ed.* **2017**, *56*, 14011.
[13] K. D. M. Rao, C. Hunger, R. Gupta, G. U. Kulkarni, M. Thelakkat, *Phys. Chem. Chem. Phys.* **2014**, *16*, 15107.
[14] J. Jung, H. Cho, S. H. Choi, D. Kim, J. Kwon, J. Shin, S. Hong, H. Kim, Y. Yoon, J. Lee, D. Lee, Y. D. Suh, S. H. Ko, *ACS Appl. Mater. Interfaces* **2019**, *11*, 15773.
[15] W. Sun, F. Jia, Z. Sun, J. Zhang, Y. Li, X. Zhang, B. Yang, *Langmuir* **2011**, *27*, 8018.
[16] M. Schöttle, M. Theis, T. Lauster, S. Hauschild, M. Retsch, *Adv. Opt. Mater.* **2023**, *11*, 2300095.
[17] M. Odziomek, F. Thorimbert, C. Boissiere, G. L. Drisko, S. Parola, C. Sanchez, M. Faustini, *Adv. Mater.* **2022**, *34*, 2204489.
[18] H. Yoon, S. Jeong, B. Lee, Y. Hong, *Nat. Electron.* **2024**, *7*, 383.
[19] E. N. Antonov, V. N. Bagratashvili, M. J. Whitaker, J. J. A. Barry, K. M. Shakesheff, A. N. Konovalov, V. K. Popov, S. M. Howdle, *Adv. Mater.* **2005**, *17*, 327.
[20] M. Schaffner, G. England, M. Kolle, J. Aizenberg, N. Vogel, *Small* **2015**, *11*, 4334.
[21] C. Von Bojnicic-Kninski, R. Popov, E. Dörsam, F. F. Loeffler, F. Breitling, A. Nesterov-Mueller, *Adv. Funct. Mater.* **2017**, *27*, 1703511.
[22] B. H. Miller, H. Liu, M. Kolle, *Nat. Mater.* **2022**, *21*, 1014.
[23] M. H. Bistervels, M. Kamp, H. Schoenmaker, A. M. Brouwer, W. L. Noorduin, *Adv. Mater.* **2022**, *34*, 2107843.
[24] L. Li, J. M. Scheiger, P. A. Levkin, *Adv. Mater.* **2019**, *31*, 1807333.

[25] L. Li, J. M. Scheiger, T. Tronser, C. Long, K. Demir, C. L. Wilson, M. A. Kuzina, P. A. Levkin, *Adv. Funct. Mater.* **2019**, *29*, 1902906.
[26] H. Kim, M. K. Abdelrahman, J. Choi, H. Kim, J. Maeng, S. Wang, M. Javed, L. K. Rivera-Tarazona, H. Lee, S. H. Ko, T. H. Ware, *Adv. Mater.* **2021**, *33*, 2008434.
[27] F. Thorimbert, M. Odziomek, D. Chateau, S. Parola, M. Faustini, *Nat. Commun.* **2024**, *15*, 1156.
[28] M. Kim, D.-J. Kim, D. Ha, T. Kim, *Nanoscale* **2016**, *8*, 9461.
[29] Z. Shu, F. Ye, P. Liu, P. Zeng, H. Liang, L. Chen, X. Zhang, Y. Chen, Z. Fan, J. Yu, H. Duan, *ACS Appl. Mater. Interfaces* **2023**, *15*, 28349.
[30] M. Kim, D. Ha, T. Kim, *Nat. Commun.* **2015**, *6*, 6247.
[31] F. L. Bargardi, H. Le Ferrand, R. Libanori, A. R. Studart, *Nat. Commun.* **2016**, *7*, 13912.
[32] E. N. Antonov, L. I. Krotova, N. V. Minaev, S. A. Minaeva, A. V. Mironov, V. K. Popov, V. N. Bagratashvili, *Quantum Electron.* **2015**, *45*, 1023.
[33] M. H. Bistervels, B. Antalicz, M. Kamp, H. Schoenmaker, W. L. Noorduin, *Nat. Commun.* **2023**, *14*, 6350.
[34] E. D. Holmstrom, D. J. Nesbitt, *J. Phys. Chem. Lett.* **2010**, *1*, 2264.
[35] J. R. Carazzone, C. L. Martin, Z. C. Cordero, *J. Am. Ceram. Soc.* **2020**, *103*, 4754.
[36] S. Zhang, O. Nahi, X. He, L. Chen, Z. Aslam, N. Kapur, Y. Kim, F. C. Meldrum, *Adv. Funct. Mater.* **2022**, *32*, 2207019.
[37] Y.-Y. Kim, J. D. Carloni, B. Demarchi, D. Sparks, D. G. Reid, M. E. Kunitake, C. C. Tang, M. J. Duer, C. L. Freeman, B. Pokroy, K. Penkman, J. H. Harding, L. A. Estroff, S. P. Baker, F. C. Meldrum, *Nat. Mater.* **2016**, *15*, 903.
[38] X. Liu, P. Feng, C. R. Agudo, H. Sun, X. Yu, J. Avaro, J. Huang, D. Hou, Q. Ran, J. Hong, J. Liu, C. Miao, H. Cölfen, *Adv. Funct. Mater.* **2024**, *34*, 2307437.
[39] M. Schöttle, T. Tran, T. Feller, M. Retsch, *Adv. Mater.* **2021**, *33*, 2101948.
[40] F. A. Nutz, M. Retsch, *Sci. Adv.* **2017**, *3*, aao5238.
[41] R. Xiong, W. Wu, C. Lu, H. Cölfen, *Adv. Mater.* **2022**, *34*, 2206509.
[42] A. F. Routh, W. B. Russel, *Ind. Eng. Chem. Res.* **2001**, *40*, 4302.
[43] J. Li, S. Luan, W. Huang, Y. Han, *Colloids Surf. A: Physicochem. Eng. Asp.* **2007**, *295*, 107.
[44] B. Hatton, L. Mishchenko, S. Davis, K. H. Sandhage, J. Aizenberg, *Proc. Natl. Acad. Sci. USA* **2010**, *107*, 10354.
[45] C.-A. Fustin, G. Glasser, H. W. Spiess, U. Jonas, *Langmuir* **2004**, *20*, 9114.
[46] P. Jan, H. Liang, R. Cheng, C. R. Greve, Y. Chuang, Y. Chiu, G. Tan, M. M. Elsenety, C. Chang, D. M. Dorrah, H. Lai, P. Chiu, S. Sun, Y. Li, E. M. Herzig, H. Chou, H. Lin, *Adv. Funct. Mater.* **2025**, *35*, 2408323.
[47] L. Helmbrecht, M. H. Futscher, L. A. Muscarella, B. Ehrler, W. L. Noorduin, *Adv. Mater.* **2021**, *33*, 2005291.
[48] Z. Li, T. Ma, S. Li, W. Gu, L. Lu, H. Yang, Y. Dai, R. Wang, *ACS Nano* **2022**, *16*, 11473.
[49] J. Gemen, J. R. Church, T.-P. Ruoko, N. Durandin, M. J. Białek, M. Weißenfels, M. Feller, M. Kazes, M. Odaybat, V. A. Borin, R. Kalepu, Y. Diskin-Posner, D. Oron, M. J. Fuchter, A. Priimagi, I. Schapiro, R. Klajn, *Science* **2023**, *381*, 1357.
[50] J. Wang, T. S. Peled, R. Klajn, *J. Am. Chem. Soc.* **2023**, *145*, 4098.
[51] J. S. Llorens, L. Barbera, A. F. Demirörs, A. R. Studart, *Adv. Mater.* **2023**, *35*, 2302868.
[52] Z. Chai, A. Childress, A. A. Busnaina, *ACS Nano* **2022**, *16*, 17641.